High resolution optical and near-IR imaging of the quadruple quasar RX J0911.4+0551[1]

I. Burud

Institut d'Astrophysique et de Géophysique, Université de Liège,

Avenue de Cointe 5, B–4000 Liège, Belgium

F. Courbin

Institut d'Astrophysique et de Géophysique, Université de Liège,

Avenue de Cointe 5, B–4000 Liège, Belgium

URA 173 CNRS-DAEC, Observatoire de Paris, F–92195 Meudon Principal Cédex, France

C. Lidman

ESO, Casilla 19001, Santiago 19, Chile

A.O. Jaunsen

Institute of Theoretical Astrophysics, University of Oslo, Pb. 1029 Blindern, N-0315 Oslo, Norway

Centre for Advanced Study, Drammensvn. 78, N-0271 Oslo, Norway

J. Hjorth

NORDITA, Blegdamsvej 17, DK-2100 Copenhagen Ø, Denmark

Centre for Advanced Study, Drammensvn. 78, N-0271 Oslo, Norway

R. Østensen

Institut d'Astrophysique et de Géophysique, Université de Liège,

Avenue de Cointe 5, B–4000 Liège, Belgium

Department of Physics, University of Tromsø, N-9037 Tromsø, Norway

M.I. Andersen, J.W. Clasen

[1]Based on observations obtained at NOT and ESO La Silla

Nordic Optical Telescope, Apartado 474, E-38700 St. Cruz de La Palma, Canary Islands, Spain

O. Wucknitz

Hamburger Sternwarte, Gojenbergsweg 112, D-21029 Hamburg, Germany

G. Meylan

ESO, Karl-Schwarzschild-Strasse 2, D-85748, Garching bei München, Germany

P. Magain[2]

Institut d'Astrophysique et de Géophysique, Université de Liège,

Avenue de Cointe 5, B–4000 Liège, Belgium

R. Stabell

Institute of Theoretical Astrophysics, University of Oslo, Pb. 1029 Blindern, 0315 Oslo, Norway

Centre for Advanced Study, Drammensvn. 78, N-0271 Oslo, Norway,

S. Refsdal

Hamburger Sternwarte, Gojenbergsweg 112, D-21029 Hamburg, Germany

Institute of Theoretical Astrophysics, University of Oslo, Pb. 1029 Blindern, N-0315 Oslo, Norway

Centre for Advanced Study, Drammensvn. 78, N-0271 Oslo, Norway

Received ______________________; accepted ______________________

[2]Maître de Recherches au Fonds National Belge de la Recherche Scientifique

ABSTRACT

We report the detection of four images in the recently discovered lensed QSO RX J0911.4+0551. With a maximum angular separation of $3.1''$, it is the quadruply imaged QSO with the widest known angular separation. Raw and deconvolved data reveal an elongated lens galaxy. The observed reddening in at least two of the four QSO images suggests differential extinction by this lensing galaxy. We show that both an ellipticity of the galaxy ($\epsilon_{\rm min} = 0.075$) and an external shear ($\gamma_{\rm min} = 0.15$) from a nearby mass has to be included in the lensing potential in order to reproduce the complex geometry observed in RX J0911.4+0551. A possible galaxy cluster is detected about $38''$ from RX J0911.4+0551 and could contribute to the X-ray emission observed by ROSAT in this field. The color of these galaxies indicates a plausible redshift in the range of 0.6-0.8.

Subject headings: galaxies: clusters: general — gravitational lensing — quasars: individual (RX J0911.4+0551)

1. Introduction

RX J0911.4+0551, an AGN candidate selected from the ROSAT All-Sky Survey (RASS) (Bade et al. 1995, Hagen et al. 1995), has recently been classified by Bade et al. (1997; hereafter B97) as a new multiply imaged QSO. B97 show that it consists of at least three objects: two barely resolved components and a third fainter one located $3.1''$ away from the other two. They also show that the spectrum of this third fainter component is similar to the combined spectrum of the two bright components. The lensed source is a radio quiet QSO at $z = 2.8$. Since RASS detections of distant radio quiet QSOs are rare, B97 pointed out that the observed X-ray flux might originate from a galaxy cluster at $z \geq 0.5$ within the ROSAT error box. We present here new optical and near-IR high-resolution images of RX J0911.4+0551 obtained with the 2.56m Nordic Optical Telescope (NOT) and the ESO 3.5m New Technology Telescope (NTT). Careful deconvolution of the data allows us to clearly resolve the object into four QSO components and a lensing galaxy. In addition, a candidate galaxy cluster is detected in the vicinity of the four QSO images. We estimate its redshift from the photometric analysis of its member galaxies.

2. Observations and reductions

We first observed RX J0911.4+0551 in the K-band with IRAC 2b on the ESO/MPI 2.2m telescope on November 12, 1997. In spite of the poor seeing conditions ($\sim 1.3''$), preliminary deconvolution of the data made it possible to suspect the quadruple nature of this object. Much better optical observations were obtained at the NOT (La Palma, Canary Islands, Spain). Three 300s exposures through the I filter, with a seeing of $\sim 0\farcs8$ were obtained with ALFOSC under photometric conditions on November 16, 1997. Under non-photometric, but excellent seeing conditions ($\sim 0\farcs5 - 0\farcs8$), three 300s I-band exposures, three 300s V-band and five 600s U-band exposures were taken with HIRAC on the night of December 3, 1997. The pixel scales for HIRAC and ALFOSC are $0\farcs1071$ and $0\farcs186$, respectively. RX J0911.4+0551 was also the first gravitational lens to be observed with the new wide field near-IR instrument SOFI, mounted on the ESO

3.5m NTT. Excellent K and J images were taken on December 15, 1997, and January 19, 1998 respectively. The 1024×1024 Rockwell detector was used with a pixel scale of $0\farcs144$.

The optical data were bias subtracted and flat-field corrected using sky-flats. Fringe-correction was also applied to the I-band data from ALFOSC. Sky subtraction was carried out by fitting low-order polynomial surfaces to selected areas of the frames. Cosmic ray removal was finally performed on the data. The infrared data were processed as explained in Courbin, Lidman & Magain (1998), but in a much more efficient way for SOFI than for IRAC 2b data, since the array used with the former instrument is cosmetically superior to the array used with the latter.

3. Deconvolution of RX J0911.4+0551

All images were deconvolved using the new deconvolution algorithm by Magain, Courbin & Sohy (1998; hereafter MCS). The sampling of the images was improved in the deconvolution process, i.e. the adopted pixel size in the deconvolved image is half the pixel size of the original frames. The final resolution adopted in each band was chosen according to the signal-to-noise (S/N) ratio of the data, the final resolution improving with the S/N.

Our NOT HIRAC data were deconvolved down to the best resolution achievable with the adopted sampling (2 pixels FWHM, i.e. $0\farcs1$), whereas the NOT/ALFOSC frames were deconvolved to a resolution of 3 pixels FWHM, i.e. $0\farcs29$. Although of very good quality, the near IR-data have a lower S/N than the optical data. The resolution was therefore limited to 5 pixels FWHM in both J and K ($0\farcs36$) in order to avoid noise enhancement.

The MCS algorithm can be used to deconvolve simultaneously a stack of individual images or to deconvolve a single stacked image. The results from the simultaneous deconvolutions are displayed in Fig. 1. The four QSO images are labeled A1, A2, A3, and B. The quality of the results was checked from the residual maps, as explained in Courbin et al. (1998). The deconvolution procedure decomposes the images into a number of Gaussian point sources, for which the program returns the positions and intensities, plus a deconvolved numerical background. In the present case, the deconvolution was also performed with an analytical De Vaucouleurs, and exponential disk galaxy profile at the position of the lensing galaxy, in order to better describe its morphology.

3.1. Results

Table 1 lists the flux of each QSO component, relative to A1, as derived from the simultaneous deconvolutions. Although the HIRAC U, V and I band data were taken during non photometric conditions, they can still be used to determine the relative fluxes between the four images of the QSO. The errors in the relative fluxes are determined from the simultaneous deconvolutions and represent the 1-σ standard deviation in the peak intensities.

When flux calibration was possible, magnitudes were calculated and the results are displayed in Table 2, which also contains the positions of the four QSO components relative to A1. The astrometric errors are derived by comparing the positions of the components in the different bands.

The deconvolved numerical background is used to determine the galaxy position from the first order moment of the light distribution. A reasonable estimate of the error on the lens position was derived from moment measurements through apertures of varying size and on several images obtained by running deconvolutions with different initial conditions. I, J, and K magnitudes for the galaxy were also estimated from the deconvolved background image by aperture photometry ($\sim 1.2''$ aperture in diameter). The numerical galaxy is elongated in all three bands and the position angle of its major axis is $\theta_G \simeq 140 \pm 5°$. In the near-IR, the galaxy looks like it is composed of a bright sharp nucleus plus a diffuse elongated disk. However we can not exclude that the observed elongation is due to an unresolved blend of two or more intervening objects. None of our two analytical profiles fit perfectly the galaxy. The De Vaucouleurs profile (e $= 1 -$ b/a $= 0.31 \pm 0.07$, $\theta_G = 130 \pm 10°$) fits slightly better than the exponential disk light distribution, but still produces residual maps with values as large as 1.5-2 per pixel, compared with a χ^2 of 2.5-5 per pixel for the exponential disk profile. The ellipticity and the position angle derived this way are very uncertain due to the low S/N of the data. Much deeper observations will be required to perform precise surface photometry of the lens(es) and to draw a definite conclusion about its (their) morphology.

3.2. Field photometry

In order to detect any intervening galaxy cluster which might be involved in the overall lensing potential and contributing to the X-ray emission observed by ROSAT, we performed I, J, and K band photometry on all the galaxies in a $2.5'$ field around the lensed QSO. A composite color image was also constructed from the frames taken through these 3 filters, in order to directly visualize any group of galaxies with similar colors, and therefore likely to be at the same redshift. The color composite is presented in Fig. 2.

Aperture photometry was carried out using the SExtractor package (LINUX version 1.2b5, Bertin & Arnouts, 1996). The faintest objects were selected to have at least 5 adjacent pixels above $1.2\sigma_{sky}$, leading to the limiting magnitudes 23.8, 21.6, and 20.0 mag/arcsec^2 in the I, J, and K bands, respectively. The faintest extended object measured in the different bands had magnitudes 23.0, 22.0, and 20.3 in I, J, and K, respectively. The color-magnitude diagram of the field was constructed from the I and K band data which give the widest wavelength range possible with our photometric data. Since the seeing was different in the two bands, particular attention was paid to the choice of the isophotal apertures fitted to the galaxies. They were chosen to be as large as possible, still avoiding too much contamination from the sky noise, as an oversized isophotal aperture would introduce. The color-magnitude diagram of the galaxies in the $2.5'$ field is displayed in Fig. 3 . Stars are not included in this plot. Note that, because of their proximity, the magnitudes of the two blended members of the cluster candidate (center of the circle in Fig. 2) might be underestimated by as much as 0.3-0.4 magnitudes in both I and K.

4. Models

In a first attempt to model the system we chose an elliptical potential of the form

$$\psi = \psi(r_{\mathrm{e}}), \tag{1}$$

$$r_{\mathrm{e}}^2 = \frac{x'^2}{(1+\epsilon)^2} + \frac{y'^2}{(1-\epsilon)^2}, \tag{2}$$

where the coordinates x' and y' are measured along the principal axes of the galaxy, whose position angle θ_{G} is a free parameter. For small ellipticities ϵ, this potential is a good approximation for elliptical mass distributions (Kassiola & Kovner 1993). Additionally, an external shear γ with direction ϕ is included. Even without assuming an explicit potential ψ, we can determine the minimal γ and ϵ needed to reproduce the observed image positions, by applying the methods given by Witt & Mao (1997). Their methods eliminate the unknown parameters of the model to find constraints for the ellipticity of the galaxy and the external shear. For the shear we predict a minimum of $\gamma_{\min} = 0.15 \pm 0.07$, while $\epsilon_{\min} = 0.075 \pm 0.034$ (both with 1σ errors). Therefore, neither ellipticity nor shear should be omitted from the modeling. To keep models simple, we used a pseudo-isothermal potential corresponding to an apparent deflection angle of

$$\boldsymbol{\alpha} = \frac{\alpha_0}{r_{\mathrm{c}} + \sqrt{r_{\mathrm{c}}^2 + r_{\mathrm{e}}^2}} \left(\frac{x}{(1+\epsilon)^2}, \frac{y}{(1-\epsilon)^2} \right), \tag{3}$$

which degenerates to a singular isothermal sphere for vanishing core-radius r_{c} and ellipticity ϵ.

The model's parameters are determined by minimizing the χ^2 given by the observed and predicted positions of the images and the galaxy. The best model leads to $\chi^2 = 0.65$ and has parameters as given in Table 3. This value is reasonable for a model with one degree of freedom (r_{c} can not be counted as a free parameter here, because without the restriction of $r_{\mathrm{c}} \geq 0$ it would become negative in the fit). The positions of the images and the galaxy in Table 3 are parameters of the model and have to be compared with the observed positions in Table 2.

As shown above, no elliptical potential without a shear, and no spherical potential with shear can reproduce the observational data. For our pseudo-isothermal model, this results in large χ^2 values of 50.5 and 63.7, respectively. These values are much too high for the two degrees of freedom.

5. Discussion

Thanks to our new high-resolution imaging data, the QSO RX J0911.4+0551 is resolved into four images. In addition, deconvolution with the new MCS algorithm reveals the lensing galaxy, clearly confirming the lensed nature of this system. The image deconvolution provides precise photometry and astrometry for all the components of the system.

Reddening in components A2 and A3 relative to A1 is observed from our U, V, and I frames that were taken within three hours on the same night. The absence of reddening in component B and the difference in reddening between components A2 and A3 suggest extinction by the deflecting galaxy. Note that although our near-IR data were obtained from 15 days to 6 weeks after the optical images, they appear to be consistent with the optical fluxes measured for the QSO images, i.e. flux ratios increase continuously with wavelength, from U to K, indicating extinction by the lensing galaxy.

We have discovered a good galaxy cluster candidate in the SW vicinity of RX J0911.4+0551 from our field photometry in the I, J, and K bands. Comparison of our color-magnitude diagram with that of a blank field (e.g., Moustakas et al. 1997) shows that the galaxies around RX J0911.4+0551 are redder than field-galaxies at an equivalent apparent magnitude. In addition, the brightest galaxies in Fig. 3 lie on a red sequence at $I - K \sim 3.3$, typical for the early type members of a distant galaxy cluster. The two dashed lines indicate our ± 0.4 color error bars at $K \sim 19$ around $I - K \sim 3.3$. Most of these galaxies are grouped in the region around a double elliptical at a distance of $\sim 38''$ and a position angle of $\sim 204^\circ$ relative to A1. This can also be seen in Fig. 2 which shows a group of red galaxies with similar colors centered on the double elliptical (in the center of the circle).

Consequently, there is considerable evidence for at least one galaxy cluster in the field. The redshift of our best candidate cluster (the one circled in Fig. 2) can be estimated from the I and K band photometry. We have compared the K-band magnitudes of the brightest cluster galaxies with the empirical K magnitude vs. redshift relation found by Aragón-Salamanca et al. (1998).

We find that our cluster candidate, with its brightest K magnitude of about ~ 17.0, should have a redshift of $z \sim 0.7$. A similar comparison has been done in the I-band without taking into account galaxy morphology. We compare the mean I magnitude of the cluster members with the ones found by Koo et al. (1996) for galaxies with known redshifts in the Hubble Deep Field and obtain a cluster redshift between 0.6 and 0.9. Finally, comparison of the $I-K$ color of the galaxy sequence with data and models from Kodama et al. (1998) confirm the redshift estimate of 0.6-0.8.

In order to calculate physical quantities from the model parameters found in section 4, we assume a simple model for the cluster which may be responsible for the external shear. For an isothermal potential, the true shear and convergence are of the same order of magnitude. As the convergence is not explicitly included in the model, the deduced shear is a reduced shear leading to an absolute convergence of $\kappa = \gamma/(1+\gamma) = 0.241$. For a cluster redshift of $z_{\rm d} = 0.7$ and with cosmological parameters $\Omega = 1$, $\lambda = 0$ this corresponds to a velocity dispersion of about $1100\,{\rm km\,s^{-1}}$ if the cluster is positioned at an angular distance of $40''$. See Gorenstein, Falco & Shapiro (1988) for a discussion of the degeneracy preventing a direct determination of κ. From the direction of the shear ϕ, (see Table 3) we can predict the position angle of the cluster as seen from the QSO to be 12° or 192°. The latter value agrees well with the position of our cluster candidate SW of the QSO images. Note also the good agreement between the position angle $\theta_{\rm G}$ derived from the observed light distribution, and the predicted position angle corresponding to our best fitting model of the lensing potential. Interestingly, this is in good agreement with Keeton, Kochanek & Falco (1998) who find that projected mass distributions are generally aligned with the projected light distributions to less than 10°.

The color of the main lensing galaxy is very similar to that of the cluster members, suggesting that it might be a member of the cluster. Using the same model for the cluster as above, assuming the galaxy at the same redshift as the cluster, and neglecting the small ellipticity of $\epsilon < 0.05$, the velocity dispersion of the lensing galaxy can be predicted from the calculated deflection angle α_0 to be of the order of $240\,{\rm km\,s^{-1}}$. Since the galaxy profile is sharp towards the nucleus in K, we cannot rule out the possibility of a fifth central image of the source, as predicted for non-singular lens models. Near-IR spectroscopy is needed to get a redshift determination of the lens and to show whether it is blended or not with a fifth image of the (QSO) source.

Some 10″ SW from the lens, we detect a small group of even redder objects. These red galaxies can be seen in Fig. 2 a few arcseconds to the left and to the right of the cross. They might be part of a second galaxy-group at a higher redshift, and with a position in better agreement with the X-ray position mentioned by B97. However, since the measured X-ray signal is near the detection limit, and the 1-σ positional uncertainty is at least 20″ , the X-ray emission is compatible with both the QSO and these galaxy groups in the field. Furthermore, this second group, at $z > 0.7$, would most likely be too faint in the X-ray domain to be detected in the RASS. In fact, even our lower redshift cluster candidate would need to have an X-ray luminosity of the order of $\mathrm{L}_{0.1-2.4\mathrm{keV}} \sim 7.10^{44} \mathrm{erg\,s^{-1}}$ (assuming a 6 keV thermal spectrum, $\mathrm{H}_0 = 50\,\mathrm{km\,s^{-1}\,Mpc^{-1}}$, $\mathrm{q}_0 = 0.5$), in order to be detected with 0.02 $\mathrm{cts\,s^{-1}}$ by ROSAT. This is very bright but not unrealistic for high redshift galaxy clusters (e.g., MS 1054-03, Donahue, Gioia, Luppino et al. 1997).

RX J0911.4+0551 is a new quadruply imaged QSO with an unusual image configuration. The lens configuration is complex, composed of one main lensing galaxy plus external shear possibly caused by a galaxy cluster at redshift between 0.6 and 0.8 and another possible group at $z > 0.7$. Multi-object spectroscopy is needed in order to confirm our cluster candidate/s and derive its/their redshift and velocity dispersion. In addition, weak lensing analysis of background galaxies might prove useful to map the overall lensing potential involved in this complex system.

The authors would like to thank A. Moorwood and J.G. Cuby for making available to us the NTT/SOFI data and the referee E.E. Falco for useful comments. We also thank S. Sohy for her help with the preliminary data analysis, T. Kodama for providing his model results for our photometric system, T.J. Broadhurst, C.R. Keeton, G. Rauw for helpful discussions and R. Sip for help in improving the figures. IB, FC and RØ are supported in part by contract ARC94/99-178 “Action de Recherche Concertée de la Communauté Française (Belgium)” and Pôle d’Attraction Interuniversitaire, P4/05 (SSTC, Belgium).

REFERENCES

Aragón-Salamanca, A., Baugh, C.M., Kauffmann, G., 1998, preprint astro-ph/9801277

Bade, N., Fink, H.H., Engels, D., et al., 1995, A&AS, 110, 469

Bade, N., Siebert, J., Lopez, S., et al., 1997, A&A, 317, L13

Bertin, E., Arnouts, S., 1996, A&AS, 117, 393

Courbin, F., Lidman, C., Magain, P., 1998, A&A, 330, 57

Donahue, M., Gioia, I., Luppino, G., et al. 1997, preprint astro-ph/9707010

Falco, E.E., Lehar, J., Shapiro, I.I., 1997, AJ, 113, 2

Gorenstein, M.V., Falco, E.E., Saphiro, I.I., 1988, ApJ, 327, 693

Hagen, H.-J., Groote, D., Engels, D., Reimers, D., 1995, A&AS, 111, 195

Kassiola, A., Kovner, I., 1993, ApJ, 417, 450

Keeton, C.R., Kochanek, C.S., Falco, E.E., 1998, preprint astro-ph/ 9708161

Kodama, T., Arimoto, N., Barger, A.J., et al., 1998, preprint astro-ph/9802245

Koo, D.C., Vogt, N.P., Phillips, A.C., et al., 1996, ApJ, 469, 535

Magain, P., Courbin, F., Sohy, S., 1998, ApJ, 494, 452

Moustakas, L.A., Davis, M., Graham, J.R., et al., 1997, ApJ, 475, 445

Witt, H.J., Mao, S., 1997, MNRAS, 291, 211

This manuscript was prepared with the AAS LATEX macros v4.0.

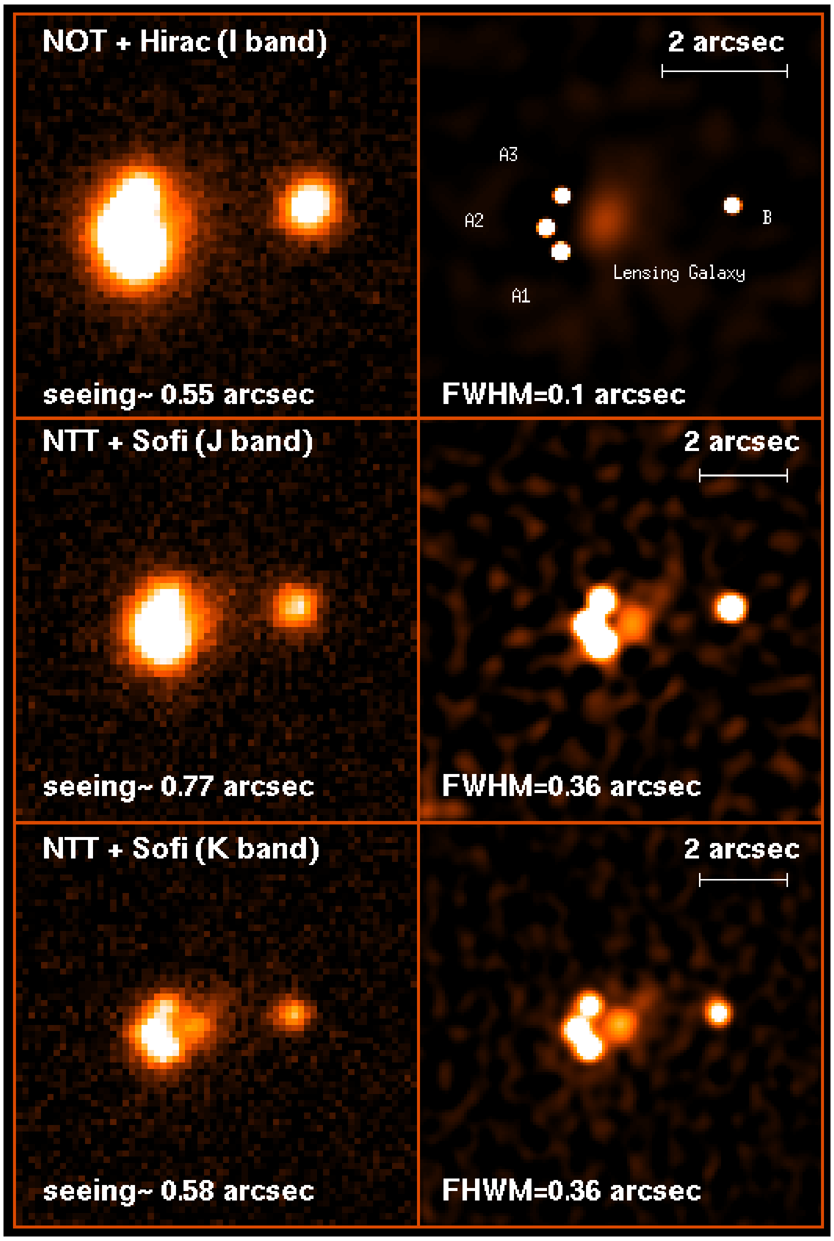

Fig. 1.— High resolution images of RX J0911.4+0551 are displayed in the left panels with, in the right panels, their corresponding deconvolved versions with improved resolution and sampling. In each band, the individual data frames are deconvolved simultaneously. [Top:] Stack of 3 NOT+HIRAC I-band image. The total exposure time is 900s. [Middle:] Stack of 9 NTT+SOFI J-band frames. The total exposure time is 1080s. [Bottom:] Stack of 19 NTT+SOFI K-band with a total exposure time of 2400s. For all the three bands the object is clearly resolved into four QSO images, labeled A1, A2, A3, and B, plus the elongated lensing galaxy. The field of the optical and near IR data are respectively $7''$ and $9''$ on a side. North is to the top and East to the left in all frames.

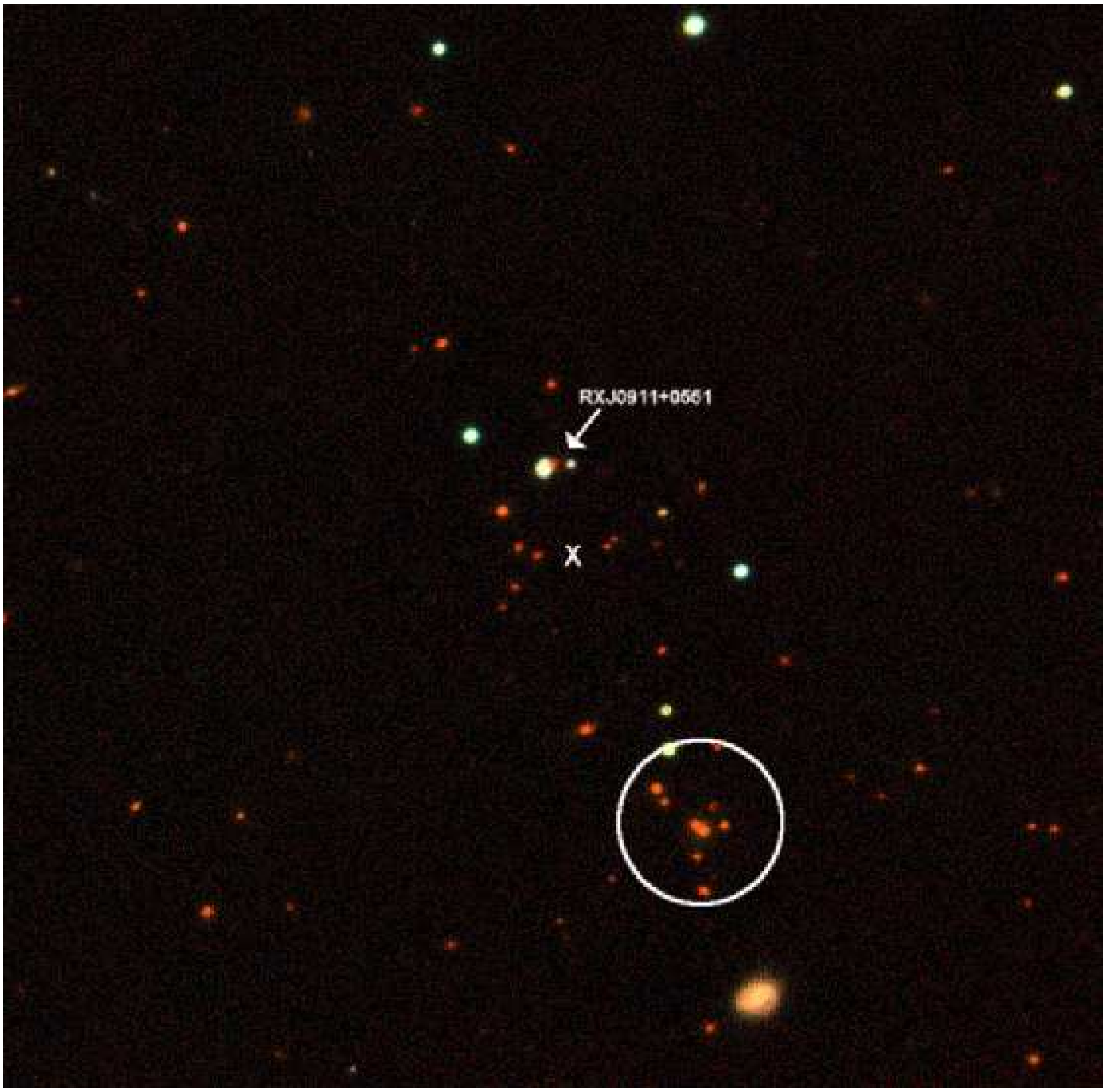

Fig. 2.— Composite image of a $2'$ field around RX J0911.4+0551. The frame has been obtained by combining our I, J and K-band data. North is up and East to the left. Note the group of red galaxies with similar colors, about $38''$ SW of the quadruple lens (circle) and the group of even redder galaxies $10''$ SW of the lens (cross).

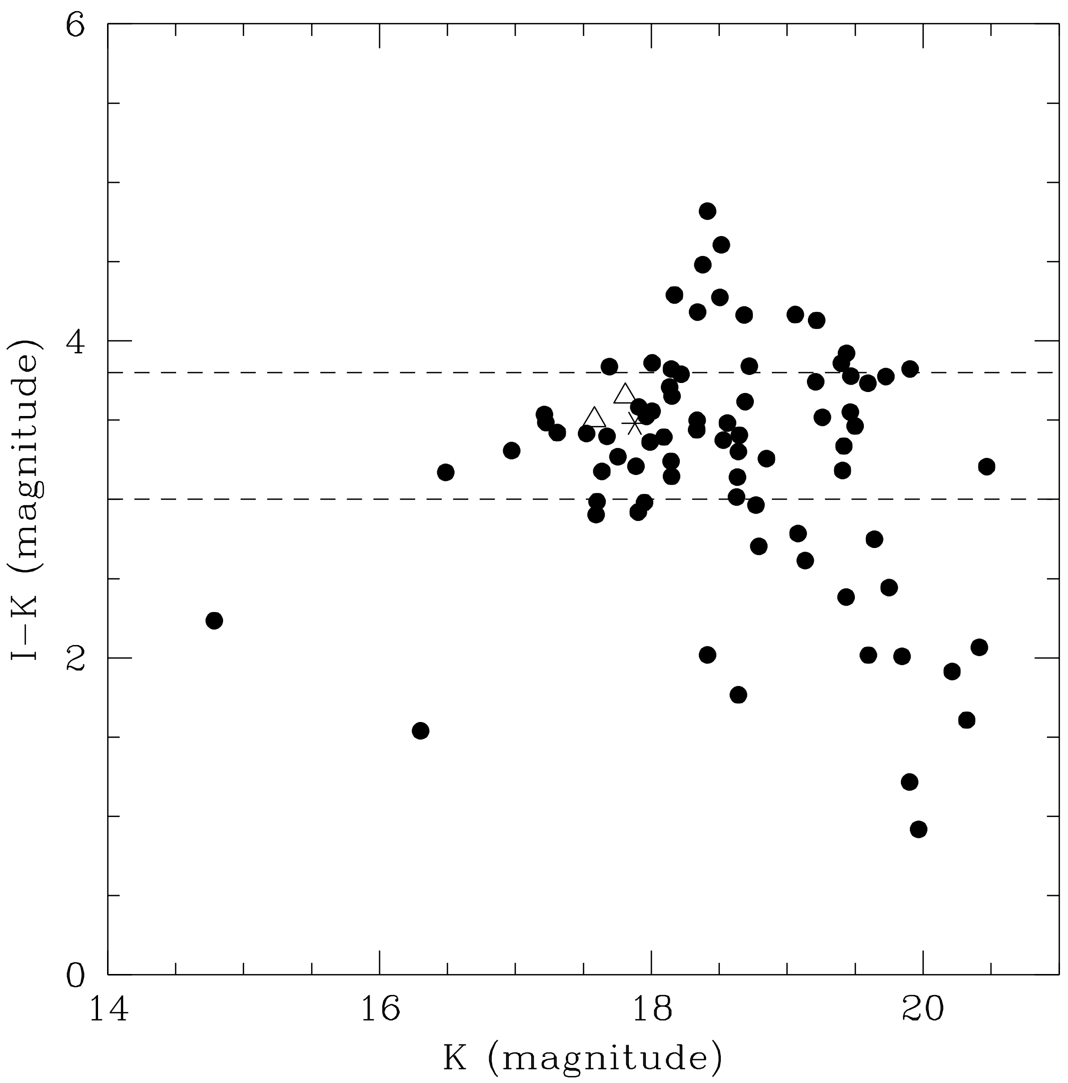

Fig. 3.— Color magnitude diagram of the 2.5′ field around RX J0911.4+0551. The lensing galaxy and many of the cluster members form the overdensity around $I - K \sim 3.3$. The lensing galaxy in RX J0911.4+0551 is marked by a star and the two blended galaxies in the center of the cluster candidate are plotted as triangles. Stars are not plotted in this diagram.

Table 1: Flux ratios for all four QSO components, relative to A1

	A2	A3	B
F_K	0.965 ± 0.013	0.544 ± 0.025	0.458 ± 0.004
F_J	0.885 ± 0.003	0.496 ± 0.005	0.412 ± 0.005
F_I	0.680 ± 0.013	0.398 ± 0.002	0.420 ± 0.003
F_V	0.587 ± 0.009	0.334 ± 0.004	0.413 ± 0.006
F_U	0.590 ± 0.013	0.285 ± 0.007	0.393 ± 0.004

Note. — Results obtained from our non-photometric data. All measurements are given along with their 1-σ errors.

Table 2: Photometric and astrometric properties of RX J0911.4+0551 and the lensing galaxy.

	A1	A2	A3	B	G
K	17.137 ± 0.020	17.308 ± 0.035	17.933 ± 0.074	18.119 ± 0.010	17.88 ± 0.12
J	17.794 ± 0.030	17.927 ± 0.029	18.556 ± 0.038	18.757 ± 0.020	19.85 ± 0.12
I	18.310 ± 0.084	18.728 ± 0.096	19.305 ± 0.133	19.197 ± 0.083	21.36 ± 0.13
$x('')$	0.000 ± 0.004	-0.259 ± 0.007	$+0.013 \pm 0.008$	$+2.935 \pm 0.002$	$+0.709 \pm 0.026$
$y('')$	0.000 ± 0.008	$+0.402 \pm 0.006$	$+0.946 \pm 0.008$	$+0.785 \pm 0.003$	$+0.507 \pm 0.046$

Note. — The astrometry is given relative to component A1 with x and y coordinates defined positive to the North and West of A1. All measurements are given along with their 1-σ errors. The 1-σ errors on the photometric zero points are 0.02 in all bands.

Table 3: Parameters of the best-fit model.

α_0	r_c	ϵ	θ_G	γ	ϕ	$\boldsymbol{\theta}_0$	$\boldsymbol{\theta}_S$
$1\farcs1061$	0	0.0476	$140\fdg5$	0.3176	$102\fdg3$	$+0\farcs7078$	$+1\farcs1459$
						$+0\farcs5440$	$+0\farcs5452$

image	x	y	amplification
A_1	$+0\farcs0000$	$-0\farcs0004$	-4.45
A_2	$-0\farcs2590$	$+0\farcs4019$	$+8.59$
A_3	$+0\farcs0130$	$+0\farcs9456$	-3.70
B	$+2\farcs9350$	$+0\farcs7850$	$+1.79$

Note. — $\boldsymbol{\theta}_0$ and $\boldsymbol{\theta}_S$ are the position of the galaxy and the source, respectively. The core radius r_c was a free parameter constrained to $r_c \geq 0$ in the modeling. The best fit lead to $r_c = 0$. Position angles θ_G and ϕ are measured from N to E. Negative amplification is due to odd parity of the image.